5-20-2006

Effect of Bio-Optical Parameter Variability and Uncertainties in Reflectance Measurements on the Remote Estimation of Chlorophyll-a Concentration in Turbid Productive Waters: Modeling Results

Giorgio Dall'Olmo
Oregon State University, giorgiod@science.oregonstate.edu

Anatoly A. Gitelson
University of Nebraska - Lincoln, agitelson2@unl.edu

Dall'Olmo & Gitelson in Applied Optics (May 20, 2006) 45(15): 3,577-3,592.

Effect of bio-optical parameter variability and uncertainties in reflectance measurements on the remote estimation of chlorophyll-a concentration in turbid productive waters: modeling results

Giorgio Dall'Olmo and Anatoly A. Gitelson

Most algorithms for retrieving chlorophyll-a concentration (*Chla*) from reflectance spectra assume that bio-optical parameters such as the phytoplankton specific absorption coefficient (a_ϕ^*) or the chlorophyll-a fluorescence quantum yield (η) are constant. Yet there exist experimental data showing large ranges of variability for these quantities. The main objective of this study was to analyze the sensitivity of two *Chla* algorithms to variations in bio-optical parameters and to uncertainties in reflectance measurements. These algorithms are specifically designed for turbid productive waters and are based on red and near-infrared reflectances. By means of simulated data, it is shown that the spectral regions where the algorithms are maximally sensitive to *Chla* overlap those of maximal sensitivity to variations in the above bio-optical parameters. Thus, to increase the accuracy of *Chla* retrieval, we suggest using spectral regions where the algorithms are less sensitive to *Chla*, but also less sensitive to these interferences. a_ϕ^* appeared to be one of the most important sources of error for retrieving *Chla*. However, when the phytoplankton backscattering coefficient ($b_{b,\phi}$) dominates the total backscattering, as is likely during algal blooms, variations in the specific $b_{b,\phi}$ may introduce large systematic uncertainties in *Chla* estimation. Also, uncertainties in reflectance measurements, which are due to incomplete atmospheric correction or reflected skylight removal, seem to affect considerably the accuracy of *Chla* estimation. Instead, variations in other bio-optical parameters, such as η or the specific backscattering coefficient of total suspended particles, appear to have minor importance. Suggestions regarding the optimal band locations to be used in the above algorithms are finally provided.

OCIS codes: 280.0280, 010.4450.

1. Introduction

This study concerns two remote-sensing algorithms designed for retrieving the chlorophyll-a concentration (*Chla*) in turbid productive waters.[1] Both algorithms use remote-sensing reflectance (R_{rs}) in the red and near-infrared (NIR) spectral regions to isolate the phytoplankton absorption coefficient in the red spectral region that is proportional to *Chla:*

$$a_\phi(\lambda_1) = m_Y(\lambda_1, \lambda_2, \lambda_3)Y(\lambda_1, \lambda_2, \lambda_3) + q_Y(\lambda_1, \lambda_2, \lambda_3), \quad (1)$$

$$a_\phi(\lambda_1) = m_Z(\lambda_1, \lambda_3)Z(\lambda_1, \lambda_3) + q_Z(\lambda_1, \lambda_3), \quad (2)$$

where $Y(\lambda_1, \lambda_2, \lambda_3) = [R_{rs}^{-1}(\lambda_1) - R_{rs}^{-1}(\lambda_2)]R_{rs}(\lambda_3)$, $Z(\lambda_1, \lambda_3) = R_{rs}^{-1}(\lambda_1)R_{rs}(\lambda_3)$ and the spectral coefficients m_Y, m_Z, q_Y, q_Z are obtained by regression analysis.[1] λ_1 is located at approximately 660–675 nm, λ_2 at approximately 700–720 nm and λ_3 in the NIR (720–750 nm) (Ref. 1).

While Eq. (1) was introduced recently,[1] Eq. (2) can be considered a special case of Eq. (1) (Ref. 1), and it has been widely used since the middle of the 1980s.[2–14] Originally, it was proposed that the optimal spectral bands for Z should be $\lambda_1 = 675$ nm and $\lambda_3 = 705$ nm, because $R_{rs}(675)$ is maximally influenced by variations in the phytoplankton absorption coefficient (a_ϕ), whereas $R_{rs}(705)$ is minimally af-

The authors are with the Center for Advanced Land Management Information Technologies, School of Natural Resources, University of Nebraska-Lincoln, 102 Nebraska Hall, Lincoln, Nebraska 68588-0517.

Received 18 October 2005; revised 28 November 2005; accepted 2 December 2005; posted 12 December 2005 (Doc. ID 65457).

0003-6935/06/153577-16$15.00/0

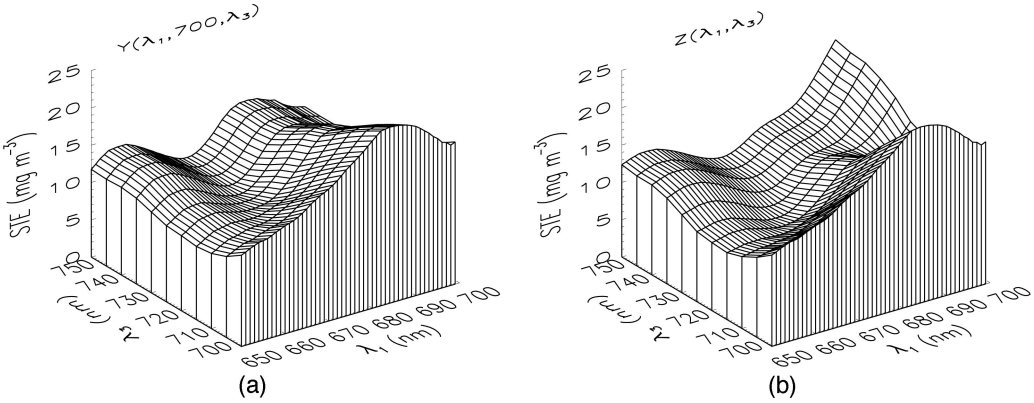

Fig. 1. Experimental standard error of *Chla* prediction as a function of λ_1 and λ_3 (recalculated from data of Ref. 1 after setting $\lambda_2 = 700$ nm): (a) three-band algorithm, (b) band-ratio algorithm.

fected by a_ϕ and thus it accounts for the variations of suspended solids in the water column.[4,5] Nevertheless, some uncertainties remain about the exact positions of the spectral bands used in the reflectance ratio *Z*. For example, several authors reported high correlations between *Chla* and band ratios that use a band at 675 nm in the denominator and one beyond 725 nm in the numerator.[8–10,12] It has also been demonstrated that band ratios have higher correlations with *Chla* when a band is used at 705 nm in the numerator and one at 665 nm in the denominator.[8,11–14] However, no explanation was given for these discrepancies with the original band formulation.

Additional experimental data showing how the spectral locations of λ_1 and λ_3 influence the accuracy of the *Chla* retrieval by Eqs. (1) and (2) have been recently presented.[1] Specifically, Eqs. (1) and (2) were regressed versus *Chla* measured analytically for each $650 \le \lambda_1 \le 700$ nm and $700 \le \lambda_3 \le 750$ nm; the resulting standard error of *Chla* estimation (STE) was used to assess how the accuracy of the retrieved *Chla* varied in the spectral space λ_1–λ_3. The STE is defined as $\mathrm{STE} = [\sum(Chla_{\mathrm{observed},i} - Chla_{\mathrm{predicted},i})^2/(N-2)]^{0.5}$, where $N-2$ are the degrees of freedom. To allow a comparison with the present study, the experimental standard error of *Chla* estimation of Ref. 1 is replotted (for $\lambda_2 = 700$ nm) as a function of λ_1 and λ_3 in Fig. 1. The three-band algorithm displayed a pronounced peak of the STE at $\lambda_1 = 683$ nm that decreased as λ_3 shifted from 700 to 750 nm [Fig. 1(a)]. Similarly, the STE of the band-ratio algorithm had a local maximum at $\lambda_1 = 683$ nm, but higher STEs were found near $\lambda_1 = 700$ nm and $\lambda_3 = 750$ nm. For both algorithms a region of minimal STE was found for $660 \le \lambda_1 \le 670$ nm and $720 \le \lambda_3 \le 740$ nm. The observed variability in the STE confirmed the findings of previous investigations,[8–14] and it was attributed (in Ref. 1) to variations in the chlorophyll-a fluorescence quantum yield (η) and, to a lesser extent, to variations in the phytoplankton specific absorption coefficient (a_ϕ^*).

The identification of the bio-optical parameters or the reflectance uncertainties responsible for the described spectral variability of the STE may allow one to assess the appropriateness of the hypotheses on which the algorithms [Eqs. (1) and (2)] were devised. Moreover, by understanding of the experimental STE, new insights about the optimal spectral locations for the bands used in the algorithms may be gained. Finally, the spectral variability of the STE may contain valuable information regarding biologically and optically significant parameters, such as the phytoplankton specific absorption coefficient or the *Chla* fluorescence quantum yield.

The objectives of this study are (1) to determine the most important sources of uncertainties in the estimation of *Chla* by use of Eqs. (1) and (2); (2) to explain the observed spectral variability of the STE; and finally (3) to find optimal spectral regions for accurate estimation of *Chla* in turbid productive waters by use of Eqs. (1) and (2). The analysis presented here is based on synthetic reflectance spectra generated by a one-dimensional semianalytical model for infinitely deep homogeneous water bodies including chlorophyll-a fluorescence[15] (Appendix A). When available, data collected in turbid productive lakes[1] were used to parameterize the model; otherwise, published values were adopted.

2. Algorithm Sensitivity to *Chla*

In the first part of the analysis the sensitivity $S_{M,Chla}$ of each algorithm (M) to variations in *Chla* was studied. To compute $S_{M,Chla}$, $R_{rs}^0(\lambda)$ was simulated by use of the semi-analytical model (Appendix A) for the nominal values of the parameters and *Chla* = 36 mg m^{-3} (Table 1 and Fig. 2). The resulting nominal reflectance spectrum is typical of turbid productive waters, with minimal values in the blue and NIR spectral regions and local maxima near 570 and 700 nm (Fig. 2). The peak near 700 nm is caused by the local minimum in total absorption that results from the sum of pure water and phytoplankton absorption at λ_{peak} (Ref. 20) (Fig. 2). Chlorophyll-a fluorescence, on the other hand, contributes a negligible

Dall'Olmo & Gitelson in Applied Optics (May 20, 2006) 45(15): 3,577-3,592.

Table 1. Nominal and Corresponding Augmented Values of the Parameters Used to Compute Figs. 5–7[a]

Parameter	Units	Nominal Value	Augmented Value
$a_\phi^*(678)$	$m^2\ mg^{-1}$	0.023 [1]	0.035 [1]
η		0.002 [16]	0.040 [16]
$a_{nap}^*(443)$	$m^2\ g^{-1}$	0.031 [17]	0.124 [arb.]
$b_{b,P}^*(550)$	$m^2\ g^{-1}$	0.0086 [18]	0.0172 [arb.]
y	–	0 [arb.]	−2 [arb.]
P	$g\ m^{-3}$	0.81 *Chla* [17]	8.1 *Chla* [1]
f/Q	sr^{-1}	–	0.2 $n^*(\lambda)$ $\langle R_{rs}(\lambda)\rangle$ [arb.]
ε	sr^{-1}	–	0.1 $R_{rs}(750)$ + $(750-\lambda)$ $\times 10^{-5}$ [arb.]
d	μm	15 [arb.]	–
c_i	$mg\ m^{-3}$	2.86×10^{-6} [19]	–
$a_{CDOM}(440)$	m^{-1}	1.0 [1]	–

[a] $n^*(\lambda)$ is the normalized (to its maximum value) average number of scattering events; $\langle R_{rs}(\lambda)\rangle$ is the median value of the reflectance spectrum (see text for details on each parameter). Numbers in square brackets indicate the references from where the values were taken; [arb.] indicates an arbitrarily selected value.

signal to the simulated remote-sensing reflectance. The ratio $Z_0(650, \lambda_3) = R_{rs}^{-1}(650)R_{rs}(\lambda_3)$ was then computed by varying λ_3 between 700 and 750 nm. This computation was repeated for each λ_1 between 650 and 699 nm and $Z_0(\lambda_1, \lambda_3)$ was obtained. The value of *Chla* was then increased by $\delta Chla = Chla(0.01)$ and the above computations were repeated to obtain $Z_{Chla}(\lambda_1, \lambda_3)$. The sensitivities $S_{Z,Chla}(\lambda_1, \lambda_3)$ and $S_{Y,Chla}(\lambda_1, 700, \lambda_3)$ (with λ_2 arbitrarily set at 700 nm) were ultimately computed as

$$S_{M,Chla} = \left| \frac{M(Chla + \delta Chla) - M(Chla)}{\delta Chla} \right|. \quad (3)$$

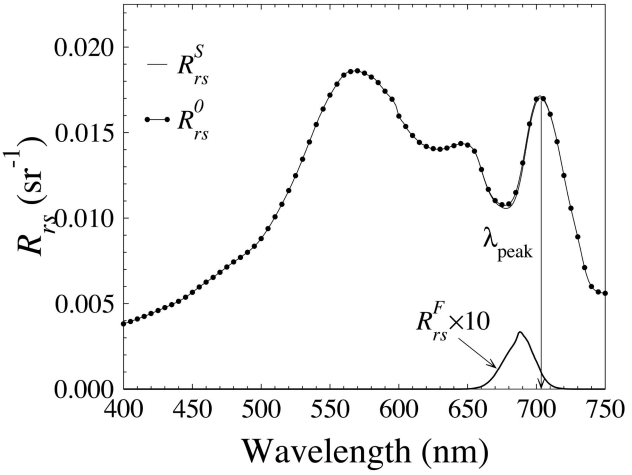

Fig. 2. Simulated R_{rs} for the nominal values of the parameters and *Chla* = 36 mg m^{-3}. $R_{rs}{}^S$ is the remote-sensing reflectance simulated with $\eta = 0$; $R_{rs}{}^0$ is the remote-sensing reflectance simulated with $\eta = 0.002$; $R_{rs}{}^F$ is the difference between $R_{rs}{}^0$ and $R_{rs}{}^S$. The location of the maximum of $R_{rs}{}^0$ in the NIR is indicated by λ_{peak}.

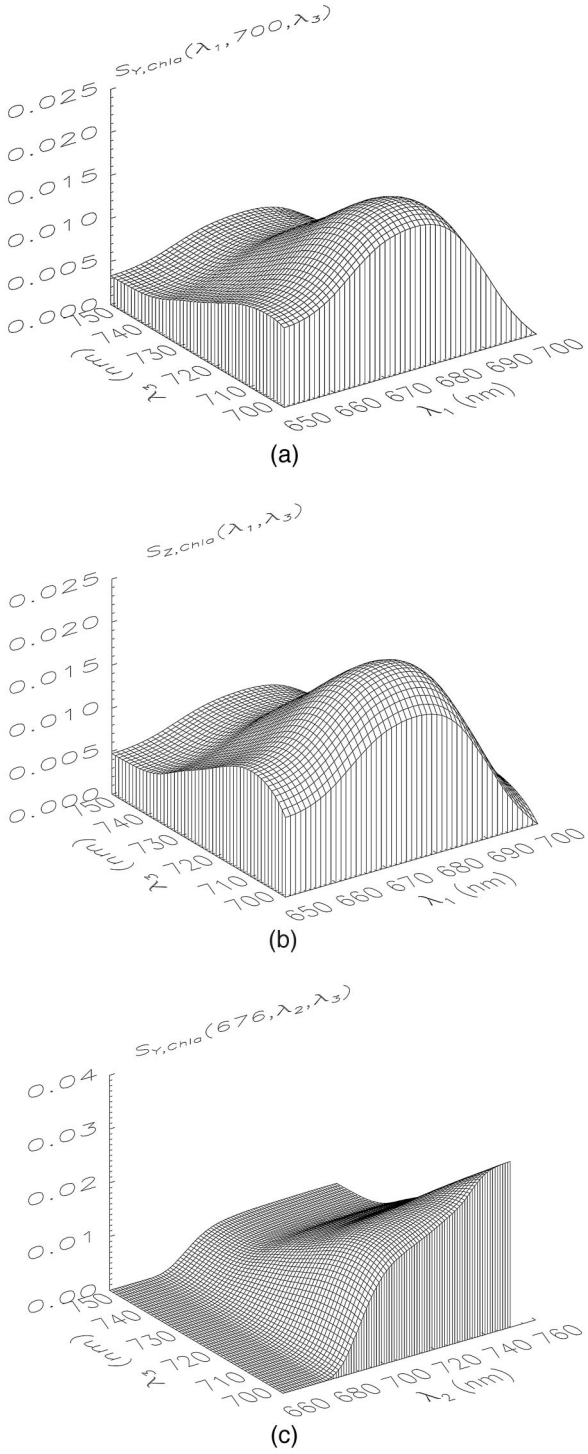

Fig. 3. Algorithm sensitivities with respect to *Chla* as a function of λ_1 and λ_3: (a) three-band algorithm, (b) band-ratio algorithm, (c) sensitivity of the three-band algorithm with respect to *Chla* as a function of λ_2 and λ_3. For these calculations *Chla* = 36 mg m^{-3}.

Figure 3 presents the results of these computations. For a fixed λ_3, Eqs. (1) and (2) were maximally sensitive to *Chla* at $\lambda_1 = 678$ nm, in correspondence with the red *Chla* absorption maximum [Figs. 3(a) and 3(b)]. For *Chla* = 36 mg m^{-3} and fixed λ_1, the sensitivity was maximal near 705 nm, at a slightly longer

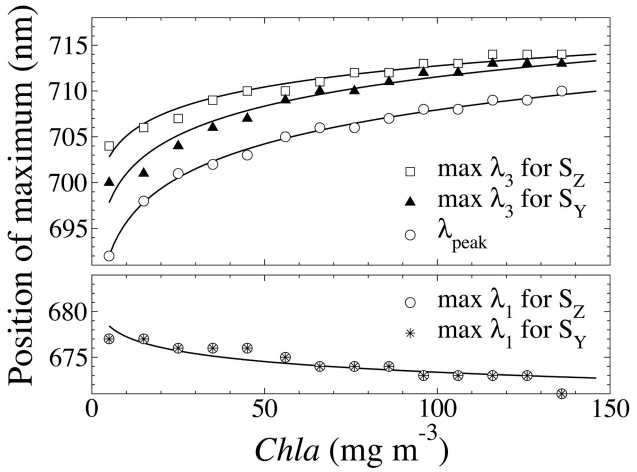

Fig. 4. λ_1 and λ_3 positions of the algorithm sensitivity maxima as functions of *Chla*. λ_{peak} is the position of the NIR reflectance maximum.

wavelength than the position of the reflectance maximum (λ_{peak} in Fig. 2); $S_{M,Chla}$ decreased as λ_3 shifted toward 750 nm. $S_{Y,Chla}$ and $S_{Z,Chla}$ were also computed for *Chla* varying between 5 and 150 mg m^{-3} and the spectral position of their maxima were plotted as a function of *Chla* (Fig. 4). While the λ_1 position of the sensitivity maxima was almost constant with respect to *Chla*, the λ_3 position shifted more than 15 nm toward longer wavelengths, following the trend of the position of the NIR reflectance maximum, λ_{peak}. Importantly, both algorithms were maximally sensitive to *Chla* at λ_3 larger than λ_{peak} because of the nonnegligible *Chla* absorption at the reflectance maximum, λ_{peak}. This implies that, to obtain maximal sensitivity to *Chla*, the λ_3 position should be shifted according to the trophic status of the water body from approximately 700 to 715 nm.

Next the sensitivity of Y is analyzed for $\lambda_1 < \lambda_2 \leq \lambda_3$, by setting $\lambda_1 = 676$ nm. First, to compute the sensitivity of Y with respect to *Chla*, the matrices $Y_0(676, \lambda_2, \lambda_3)$ and $Y_{Chla}(676, \lambda_2, \lambda_3)$ were calculated following the procedure previously described, for *Chla* = 36 mg m^{-3}. Then, $S_{Y,Chla}(676, \lambda_2, \lambda_3)$ was computed with Eq. (3) [Fig. 3(c)]. From the definition of Y, we see that, as $\lambda_2 \to \lambda_1$, $Y \to 0$, while as $\lambda_2 \to \lambda_3$, $Y \to R_{rs}(\lambda_3)/R_{rs}(\lambda_1) - 1$, i.e., $Y \propto Z$. Therefore, the sensitivity of Y to *Chla* is always lower than that of Z, the band-ratio algorithm. This is demonstrated in Fig. 3(c), where the sensitivity of Z is represented by values of $S_{Y,Chla}$ with $\lambda_2 = \lambda_3$.

3. Variations in *Chla* Due to Variations in Bio-Optical Parameters

A. Δ*Chla* Calculations

The second step of the study concerned the analysis of the errors in *Chla* estimation introduced by variations in bio-optical parameters. These errors were estimated as follows. Using the nominal values of the parameters (Table 1), $Z_0(\lambda_1, \lambda_3)$ and $Y_0(\lambda_1, 700, \lambda_3)$ were calculated for *Chla* ranging between 5 and 150 mg m^{-3} in steps of 5 mg m^{-3}, and for $650 \leq \lambda_1 \leq 699$ nm and $700 \leq \lambda_3 \leq 750$ nm. Then, for each pair of λ_1 and λ_3, the relationship between *Chla* and $Z_0(\lambda_1, \lambda_3)$ and between *Chla* and $Y_0(\lambda_1, 700, \lambda_3)$ were fitted by a least-squares method to third-order polynomials:

$$Chla = \sum_{n=0}^{3} \tau_n(\lambda_1, \lambda_2, \lambda_3)[Y(\lambda_1, \lambda_2, \lambda_3)]^n, \quad (4)$$

$$Chla = \sum_{n=0}^{3} \kappa_n(\lambda_1, \lambda_3)[Z(\lambda_1, \lambda_3)]^n. \quad (5)$$

Equations (5) and (4) allowed us to predict *Chla* by knowing the (simulated) values of $Z(\lambda_1, \lambda_3)$ or $Y(\lambda_1, 700, \lambda_3)$ at any wavelength $650 \leq \lambda_1 \leq 699$ nm and $700 \leq \lambda_3 \leq 750$ nm, with a maximum relative error of less than 1%. The third order polynomials were adopted because the simulated values of Y and Z were nonlinearly related to *Chla* (not shown). This nonlinearity was not evident in the experimental data set[1] probably because of the inherent variance of the real-world observations. Thus the use of high-order polynomials [Eqs. (4) and (5)] allowed us to focus on errors in *Chla* estimation that were due to variations in the bio-optical parameters and reflectance uncertainties rather than on errors in *Chla* related to the above nonlinearity.

The Δ*Chla* that is due to a variation in a bio-optical parameters, p, was computed as the relative change in the *Chla* predicted by the algorithm M, i.e.,

$$\Delta Chla(M_p) = \left| \frac{Chla(M_0) - Chla(M_p)}{Chla(M_0)} \right|, \quad (6)$$

where $Chla(M_0)$ and $Chla(M_p)$ are the *Chla* values calculated by Eq. (4) or (5) from $M_0(\lambda_1, \lambda_3)$ and $M_p(\lambda_1, \lambda_3)$, respectively. For example, to compute the relative change in the *Chla* predicted by Z that was due to variations in the chlorophyll-a fluorescence quantum yield, η was increased by the amount indicated in Table 1 and the matrix $Z_\eta(\lambda_1, \lambda_3)$ was calculated for a fixed *Chla*. Then the relative change in the predicted *Chla* that was due to a variation in η was computed for each λ_1 and λ_3 by use of Eq. (6). Note that, for a fixed *Chla*, the denominator on the right-hand side of Eq. (6) is constant for each λ_1 and λ_3 and it is introduced only to normalize the change in *Chla*.

The following bio-optical parameters were investigated (Table 1):

- the phytoplankton specific absorption coefficient (described by ρ', see Appendix A),
- the chlorophyll-a fluorescence quantum yield (η),
- the specific absorption coefficient of nonalgal particles (a_{nap}^*),
- the total particle specific backscattering coefficient ($b_{b,P}^*$),
- the spectral slope (y) of $b_{b,P}^*$,

- the concentration of total suspended particles (P).

Figures 5–7 report the results of the above calculations for the first five bio-optical parameters and for $Chla$ = 10, 36, and 100 mg m^{-3}, respectively. Figure 8 presents the results for variations in P. The nominal reflectance spectra, as well as the spectra resulting after each parameter was augmented, are also presented. The resulting $\Delta Chla$ are described below.

B. $\Delta Chla$ Due to Variations in ρ' [Figs. 5(a)–5(c), 6(a)–6(c), 7(a)–7(c)]

- R_{rs} varies mostly in the regions where phytoplankton pigment absorption is maximal.
- $\Delta Chla$ shows a strong λ_1 dependence, with a maximum at 678 nm, in the region of the red $Chla$ absorption maximum.
- $\Delta Chla$ shows λ_3 dependence mostly when λ_3 is near 700 nm; an exception is made for Y at $Chla$ = 10 mg m^{-3}. Such dependence increases with $Chla$.
- As $\lambda_3 \rightarrow 750$ nm, $\Delta Chla$ decreases. Such a decrease is more pronounced near 700 nm, but it asymptotically levels out at longer λ_3.
- In general $\Delta Chla(Y_{\rho'}) > \Delta Chla(Z_{\rho'})$.
- As $Chla$ increases, $\Delta Chla$ increases, especially for λ_1 = 678 nm and λ_3 = 700 nm. Remarkably, at longer λ_3, the dependence of $\Delta Chla$ on $Chla$ is much weaker.

C. $\Delta Chla$ Due to Variations in η [Figs. 5(d)–5(f), 6(d)–6(f), 7(d)–7(f)]

- R_{rs} changes only in correspondence to the chlorophyll-a fluorescence emission around 687 nm.
- $\Delta Chla$ shows a strong λ_1 dependence, with a maximum near 687 nm and a minimum near 670 nm.
- For $\lambda_1 > 670$ nm, the λ_3 dependence is limited to the low $Chla$ case [Figs. 5(e) and 5(f)], with a maximum near λ_3 = 700 nm.
- For $\lambda_1 < 670$ nm, $\Delta Chla$ has a maximum near λ_3 = 700 nm, decreasing toward longer λ_3, except in the case of the three-band algorithms at $Chla$ = 10 mg m^{-3}.
- As $Chla$ increases, $\Delta Chla$ decreases.

D. $\Delta Chla$ Due to Variations in a_{nap}* [Figs. 5(g)–5(i), 6(g)–6(i), 7(g)–7(i)]

- R_{rs} is variable throughout the spectrum, but differences are more pronounced in the blue-green region.
- $\Delta Chla \leq 0.25$ for a variation in a_{nap}* of a factor of 4.

E. $\Delta Chla$ Due to Variations in $b_{b,P}$* [Figs. 5(j)–5(l), 6(j)–6(l), 7(j)–7(l)]

- While R_{rs} changes by a factor of 2 in the visible and NIR spectral regions, $\Delta Chla \leq 0.2$.
- For $Chla < 100$ mg m^{-3}, $\Delta Chla(Y) < \Delta Chla(Z)$, especially if $\lambda_3 > 730$ nm.

F. $\Delta Chla$ Due to Variations in y [Figs. 5(m)–5(o), 6(m)–6(o), 7(m)–7(o)]

- R_{rs} as large as 30%–100% are found in the red and NIR regions, with largest relative variations in the NIR.
- Minimal $\Delta Chla$ are found for λ_1 = 680 nm and λ_3 = 700 nm.
- $\Delta Chla(Y)$ decreases as λ_3 shifts toward longer wavelengths and as λ_1 shifts toward 650 nm.
- $\Delta Chla$ increases as $Chla$ decreases.

G. $\Delta Chla$ Due to Variations in P (Fig. 8)

- R_{rs} varies by a factor of 4 to a factor of 6 in the red–NIR spectral region.
- $\Delta Chla[Y(675, 700, 750)]$ is considerably lower than $\Delta Chla[Z(675, 750)]$ for $Chla$ = 10 mg m^{-3} (0.16 vs. 1.38, respectively) and for $Chla$ = 36 mg m^{-3} (0.07 vs. 0.69, respectively).
- $\Delta Chla$ = 100 mg m^{-3}, $\Delta Chla[Y(675, 700, 750)]$ = 0.36, while $\Delta Chla[Z(675, 750)]$ = 0.16.

4. Variations in *Chla* Due to Variations in R_{rs}

A. $\Delta Chla$ Due to Variations in f/Q

One of the assumptions on which Eqs. (1) and (2) are based is that the f/Q factor, describing the anisotropy of the reflected radiant field,[21] does not change with wavelength. In reality, this factor typically introduces wavelength-dependent changes in R_{rs} of ~10% for nadir viewing angles, as for the data from which the STE of Fig. 1 was computed.[21,22] The wavelength dependency of f/Q is due to the almost proportional relationship between f/Q and $n(\lambda) = 1 + b(\lambda)/a(\lambda)$, the average number of scattering events that photons undergo before emerging from the water.[21]

The semianalytical model that was used to simulate R_{rs} in this study does not allow us to compute variations in R_{rs} that are due to changes in the f/Q factor because it is one dimensional. Therefore we simulated changes in R_{rs} that are due to variations in f/Q as $\Delta R_{rs}(\lambda) = 0.2n^*(\lambda)\langle R_{rs}(\lambda)\rangle$. Here $n^*(\lambda)$ is $n(\lambda)$ normalized to its maximum value and provides the spectral dependency of ΔR_{rs}; $\langle R_{rs}(\lambda)\rangle$ is the median value of the nominal reflectance spectrum and provides the intensity of ΔR_{rs}. The 0.2 factor allowed us to set the average value of $\Delta R_{rs}(\lambda)$ to approximately 10% of R_{rs}. The results of these calculations (not shown) demonstrated that the effect of typical variations of f/Q on the $Chla$ predicted by Y and Z is negligible (maximal $\Delta Chla$ of the order of 5% for $Chla \geq 36$ mg m^{-3}), even though it appears to slightly increase for $Chla$ = 10 mg m^{-3} ($\Delta Chla$ of the order of 15%).

B. $\Delta Chla$ Due to Errors in the Correction of Atmospheric Effects or Skylight Reflection

Reflectance data measured from satellite sensors are often affected by uncertainties that are due to atmospheric correction schemes that do not account for blue-absorbing aerosols or erroneously estimate aerosol path radiance. On the other hand, above-water

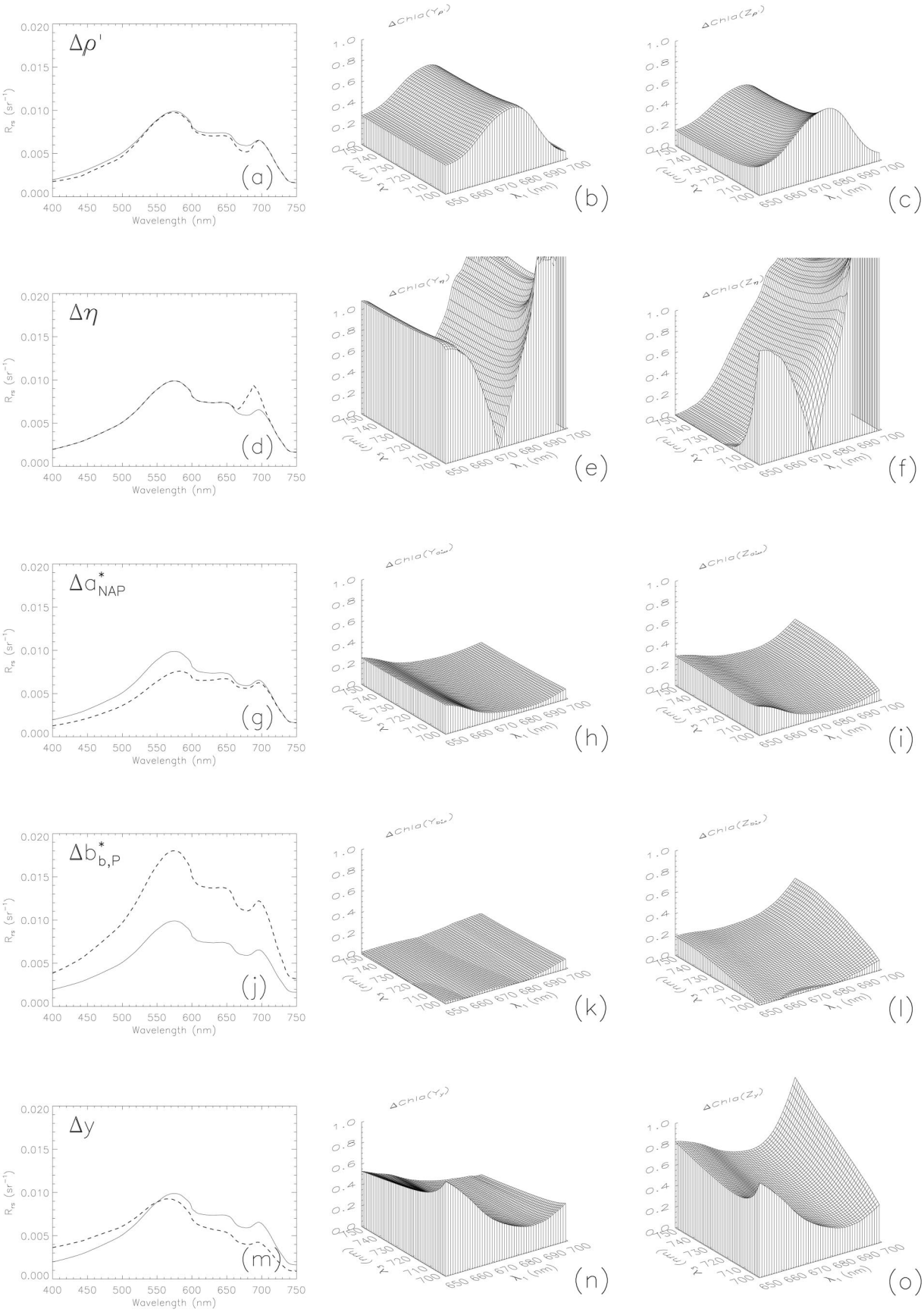

Fig. 5. R_{rs} spectra and $\Delta Chla$ computed for the variations in bio-optical parameters described in Table 1 and for $Chla = 10$ mg m^{-3}. First column: nominal reflectance spectrum (solid curve) and reflectance spectrum computed after the indicated bio-optical parameter was augmented (dashed curve). Second column: $\Delta Chla$ calculated for the three-band algorithm (Y). Third column: $\Delta Chla$ calculated for the band-ratio algorithm (Z).

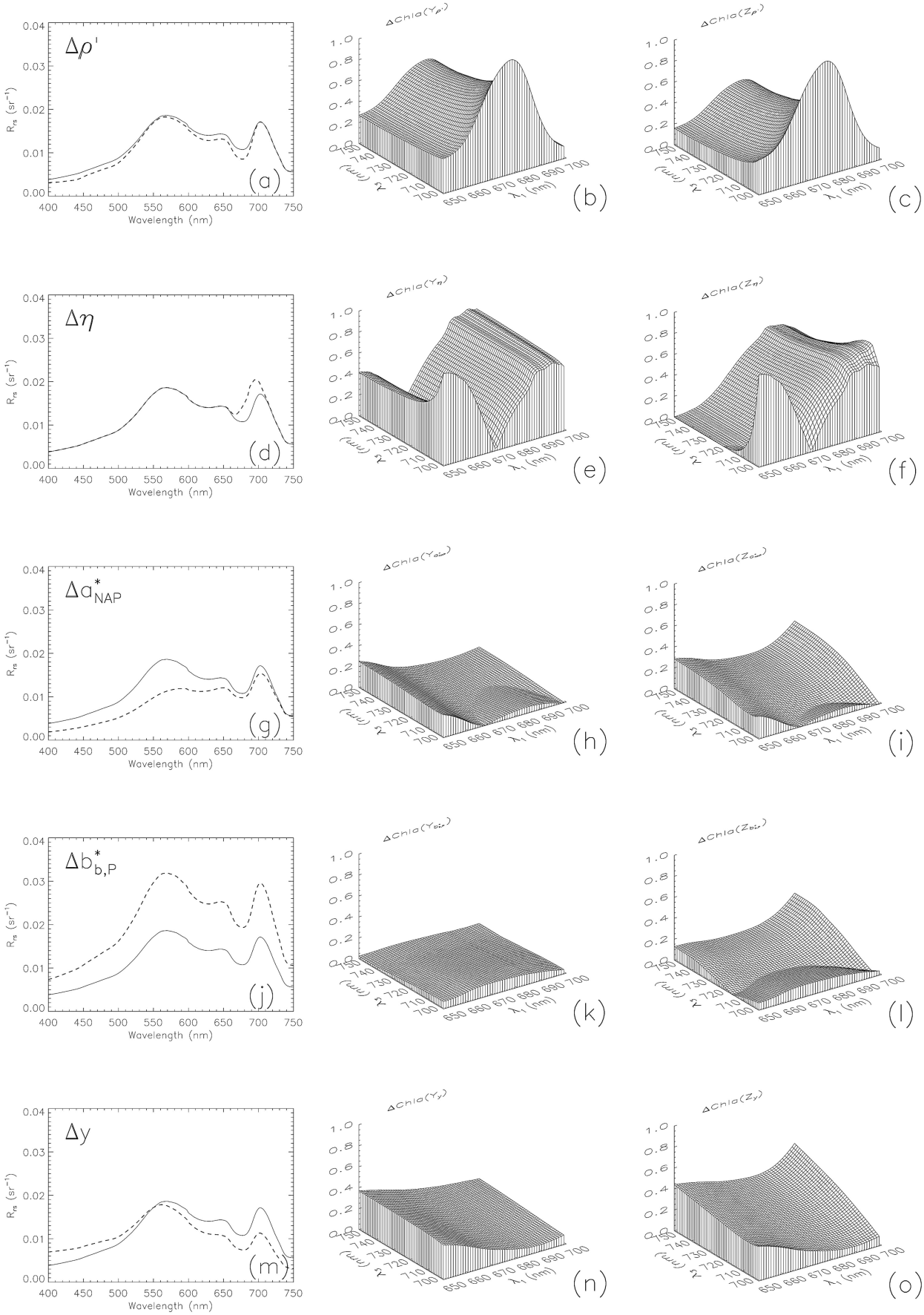

Fig. 6. As Fig. 5, but for $Chla = 36$ mg m^{-3}.

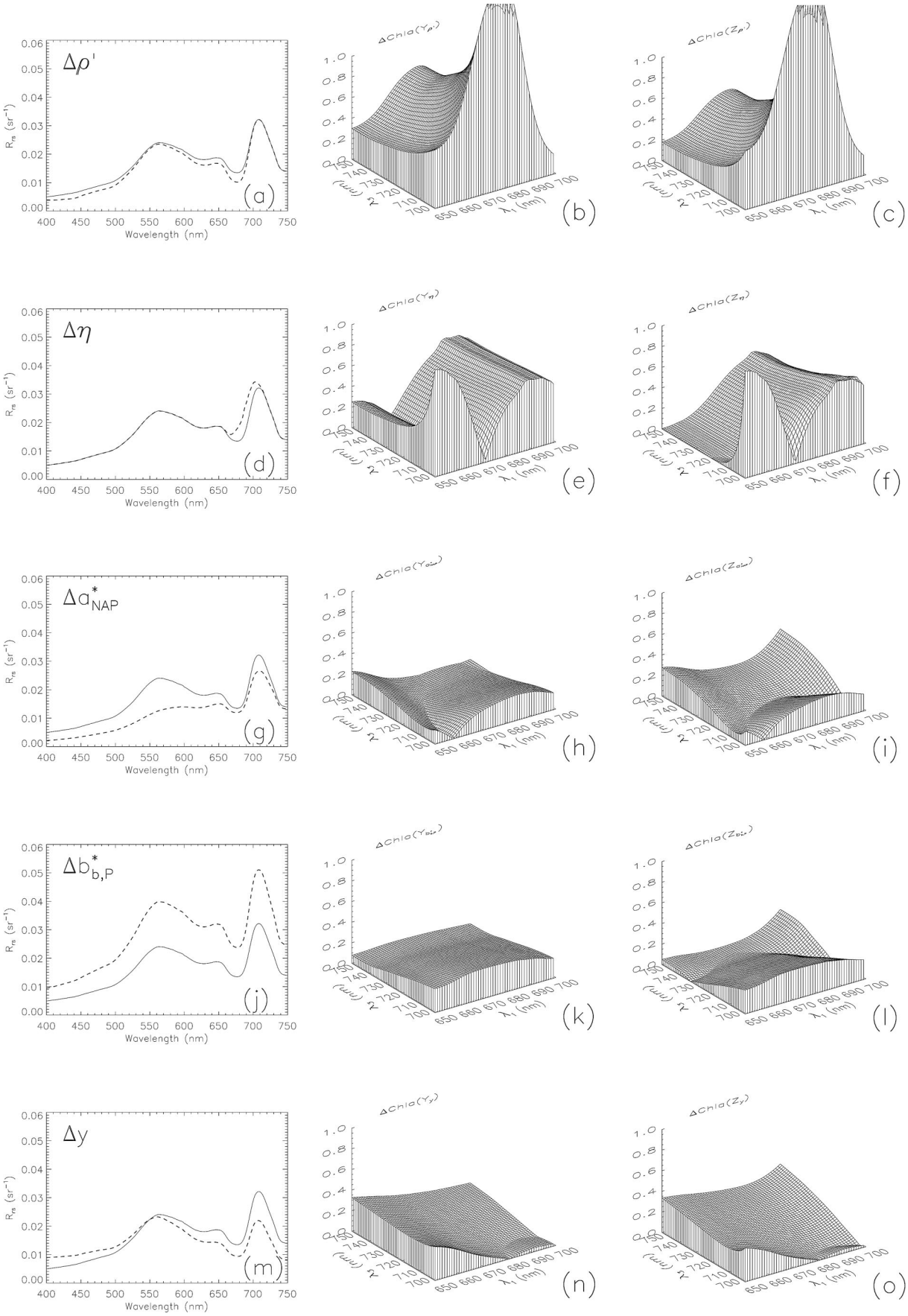

Fig. 7. As Fig. 6, but for $Chla = 100$ mg m^{-3}.

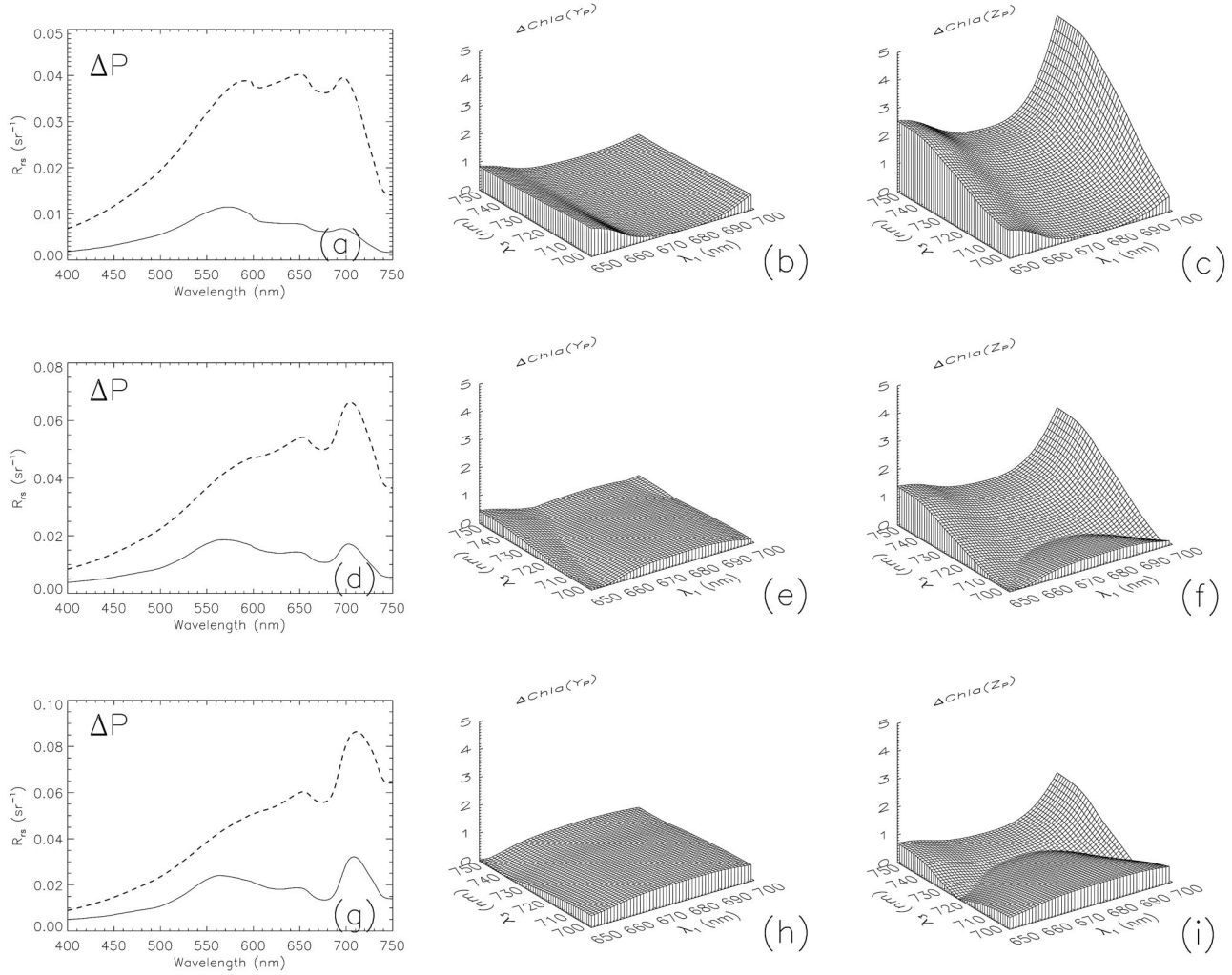

Fig. 8. R_{rs} spectra and $\Delta Chla$ computed for the variations in P described in Table 1 for three $Chla$ levels: top row, $Chla = 10$ mg m^{-3}; middle row, $Chla = 36$ mg m^{-3}; bottom row, $Chla = 100$ mg m^{-3}. First column, R_{rs} spectra; second column: three-band algorithm (Y); third column: band-ratio algorithm (Z).

remote-sensing reflectance data collected *in situ* can be influenced by errors related to the subtraction of surface skylight reflection. The influence of surface-reflected skylight on R_{rs} depends on a variety of parameters, among which are cloud cover, wind speed, and solar and viewing geometries.[23] The net effect of the uncertainties in R_{rs} that are due to atmospheric correction and surface skylight removal is a variation in R_{rs} that, in general, has a smooth wavelength dependence.[23,24] To analyze the effect of these uncertainties on the $Chla$ predicted by Eqs. (1) and (2), we assumed that the above errors vary linearly over the relatively narrow range investigated (650–750 nm). We arbitrarily expressed the variation in R_{rs} as $\Delta\varepsilon(\lambda) = 0.1\,R_{rs}(750) + (750 - \lambda) \times 10^{-5}$, where $0.1\,R_{rs}(750)$ is the magnitude of the R_{rs} deviation at 750 nm and $(750 - \lambda) \times 10^{-5}$ describes the spectral dependence of ΔR_{rs}. Figure 9 shows that, in the red–NIR spectral region, $\Delta Chla$ was considerably affected by these R_{rs} variations since it varied by approximately 20% as R_{rs} changed by approximately 10%. Similar results were obtained when the sign of ε was inverted (not shown).

5. Effect of Anomalous Diffraction on $\Delta Chla$

Anomalous diffraction refers to the spectral dependence of the real part of the refractive index, and thus of the (back)scattering coefficient, in the vicinity of absorption bands.[25] Phytoplankton pigment absorption has a local maximum near 675 nm that should cause $b_{b,\phi}$ to vary spectrally. Because the spectral independence of b_b in the red and NIR regions is one of the assumptions on which Y and Z were developed, this section is dedicated to the analysis of the influence of anomalous diffraction on $\Delta Chla$.

To accomplish this objective, we computed remote-sensing reflectance for $Chla = 36$ mg m^{-3} by using phytoplankton specific inherent optical properties derived by Mie theory[26] and inherent optical properties of the other constituents computed as for the rest of this paper (Appendix A). First, we set $b_b = b_{b,w} + b_{b,\phi} + b_{b,P}$, and therefore the resulting total back-

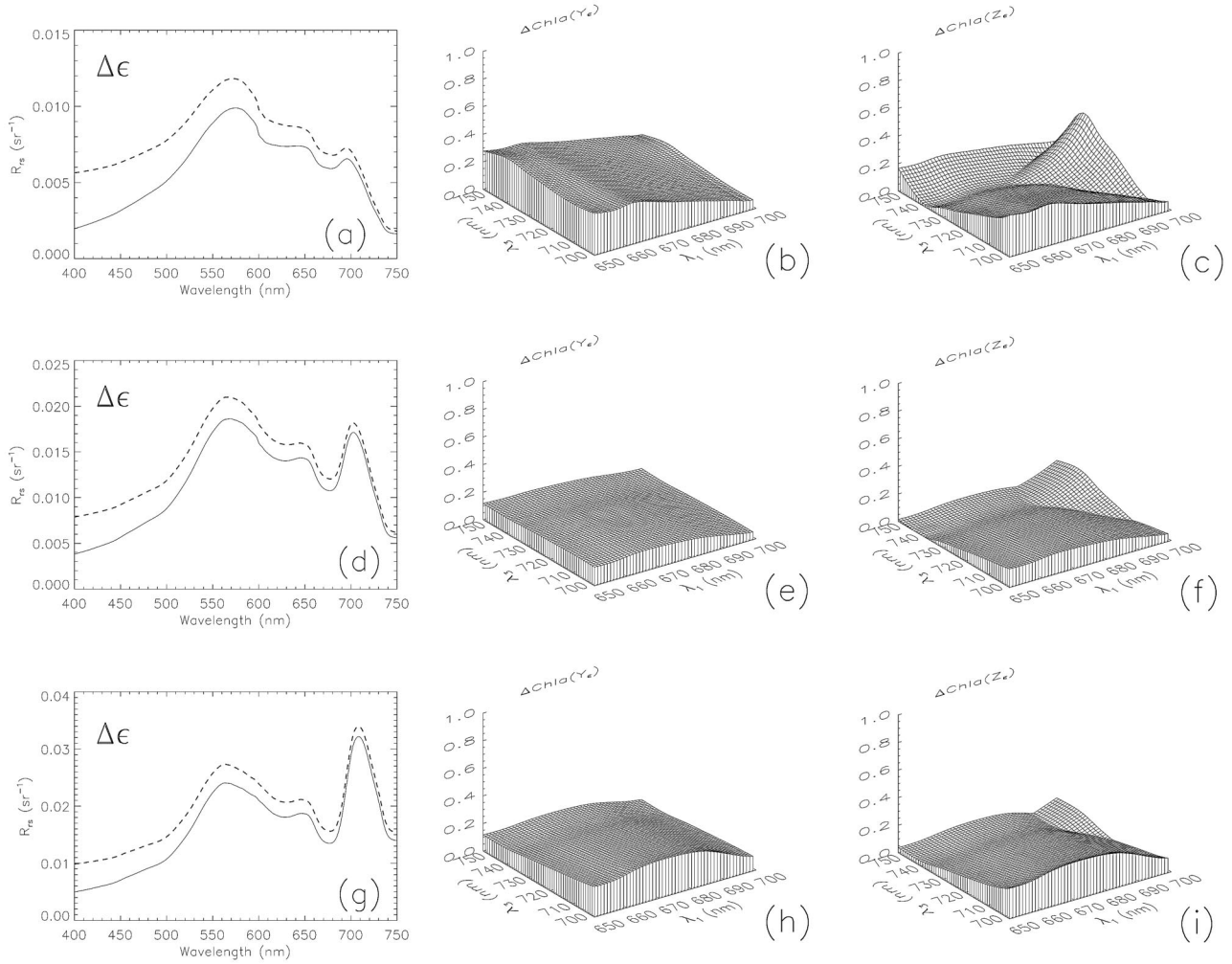

Fig. 9. R_{rs} spectra and $\Delta Chla$ computed for the variations in ε described in Table 1 for three *Chla* levels: top row, *Chla* = 10 mg m^{-3}; middle row, = 36 mg m^{-3}; bottom row, *Chla* = 100 mg m^{-3}. First column, *Chla* R_{rs} spectra; second column, three-band algorithm (*Y*); third column, band-ratio algorithm (*Z*).

scattering coefficient was slightly larger than that for the other simulations presented in this paper. To include another extreme case, we then computed b_b, neglecting $b_{b,P}$, i.e., $b_b = b_{b,w} + b_{b,\phi}$. *Y* and *Z*, as well as the coefficients of the fitting equations [see Eqs. (4) and (5)] and $\Delta Chla(M_{\mathrm{Mie}})$ that were due to variations in the average diameter of the phytoplankton cells from 3.36 to 6.00 μm, were finally computed as described in Subsection 3.A. Inputs for these calculations were the complex refractive index of phytoplankton (*Platymonas suecica*, taken from Ref. 27) and the number size distribution function that was represented as a Gaussian peak with a central diameter of 3.36 μm (Ref. 27) and a standard deviation of 0.5 μm. We also repeated the calculations for a central diameter of 6.00 μm. To reduce computation time, only wavelengths from 650 to 750 nm were considered. The simulated phytoplankton specific absorption and backscattering coefficients are presented in Fig. 10. As the cell diameter increased from 3.36 to 6.00 μm, a_ϕ* decreased. The largest difference between a_ϕ*(3.36 μm) and a_ϕ*(6.00 μm) occurred at 675 nm. The relative decrease between $b_{b,\phi}$*(3.36 μm) and $b_{b,\phi}$*(6.00 μm) was larger than that of a_ϕ* and showed a different spectral shape with inflections at 675 and 720 nm (Fig. 10, inset). The input parameters for the above calculations were taken from the literature; thus the obtained phytoplankton inherent optical properties were different from those used elsewhere in this study. However, the results obtained here are still qualitatively comparable with the experimental error (see below).

To facilitate the comparison, the experimental STE and $\Delta Chla(M_{\mathrm{Mie}})$ are presented for a fixed λ_1 (i.e., 660 and 670 nm) as functions of λ_3 in Fig. 11. The experimental STE showed a nonmonotonic behavior with local minima at 720 and 730 nm for λ_1 = 660 and 670 nm, respectively [Fig. 11(a)]. On the contrary, $\Delta Chla(M_{\mathrm{Mie}})$ computed including $b_{b,P}$ decreased monotonically from λ_3 = 700 nm toward longer wavelengths [Fig. 11(b)]. However, when $b_{b,P}$ was neglected, $\Delta Chla(M_{\mathrm{Mie}})$ exhibited a local minimum near 720 nm and qualitatively resembled the observed STE [compare Figs. 11(a) and 11(c)]. This

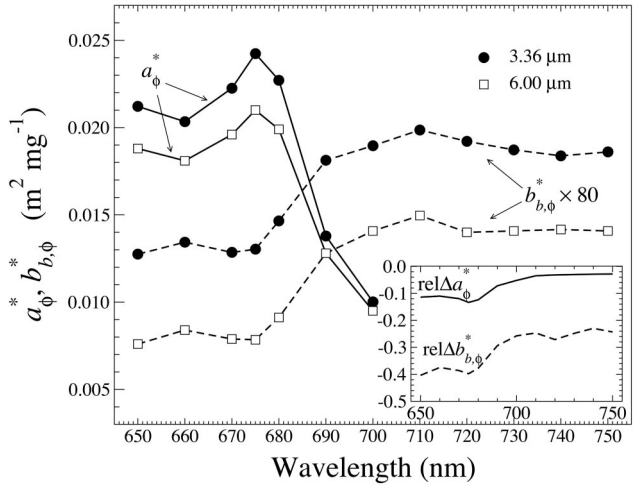

Fig. 10. Phytoplankton specific absorption and backscattering coefficients simulated by use of Mie theory for a Gaussian number size distribution with a standard deviation of 0.5 μm and two central diameters: 3.36 μm (filled circles) and 6.00 μm (open squares). To demonstrate the spectral variability, the relative change in each specific inherent optical property is presented in the inset.

implies that the average b_b^* coefficient of the experimental data set may have been spectrally dependent, as was found in other studies.[28,29]

To understand how variations in $b_{b,\phi}^*$ and a_ϕ^* separately affected $\Delta Chla$, we repeated the above calculations, first by keeping a_ϕ^* constant and by varying only $b_{b,\phi}^*$, and then by keeping $b_{b,\phi}^*$ constant, but a_ϕ^* variable. These computations were repeated with $b_{b,P}$ both accounted for and neglected. Moreover, to analyze for potential $\Delta Chla$ of opposite signs, the absolute value in Eq. (6) was not evaluated for these simulations. Variations in $b_{b,\phi}^*$ affected significantly the error in *Chla* estimation only when $b_{b,\phi}^*$ contributed a considerable fraction of the total b_b [Figs. 12(a) and 12(b)], as for example during algal blooms. In such cases, the $\Delta Chla$ that was due to variations in $b_{b,\phi}^*$ was larger than that due to variations in a_ϕ^* and it was also characterized by a maximum near 675 nm that decreased in intensity as λ_3 shifted from 700 nm toward longer wavelengths. Furthermore, variations in $b_{b,\phi}^*$ and a_ϕ^* had opposite signs and therefore compensated for each other. Instead, when the total b_b was dominated by nonalgal particles, variations in a_ϕ^* were responsible for most of the $\Delta Chla$ [Figs. 12(c) and 12(d)]. Finally, we note that no qualitative differences were found by using *Chla* values different from 36 mg m^{-3} (not shown).

6. Comparison of Simulated and Experimental Results

The experimental STE in Fig. 1 originates from the sum of several uncertainties owing to variations of different bio-optical parameters, use of approximate relationships for extracting $a_\phi(\lambda_1)$ from R_{rs} [Eqs. (1) and (2)], and errors associated with reflectance measurements. Our objective in this section is to attempt

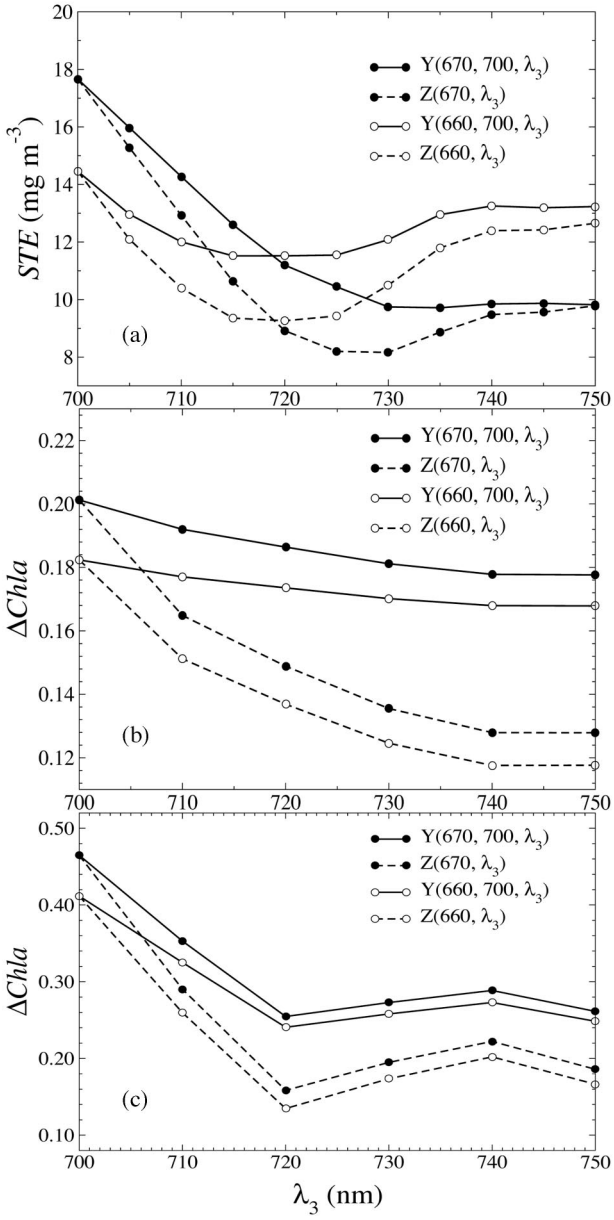

Fig. 11. Comparison between experimental STE and simulated $\Delta Chla$: (a) experimental STE, (b) $\Delta Chla$ computed taking into account the contribution of backscattering by nonalgal particles; (c) $\Delta Chla$ computed neglecting the contribution of backscattering by nonalgal particles. *Chla* was set at 36 mg m^{-3}.

to interpret the observed STE in light of the simulations presented above.

The experimental STE in Fig. 1 can be seen as an average absolute *Chla* residual, and its spectral behavior can thus be qualitatively compared to that of the simulated $\Delta Chla$. The most evident characteristic of the experimental STE is the presence of a maximum centered at $\lambda_1 = 683$ nm and $\lambda_3 = 700$ nm (Fig. 1). This maximum decreases in magnitude as λ_3 moves toward longer wavelengths and almost disappears in the band-ratio algorithm [Fig. 1(b)].

According to the analysis presented in the previous sections, such a maximum is likely related to the

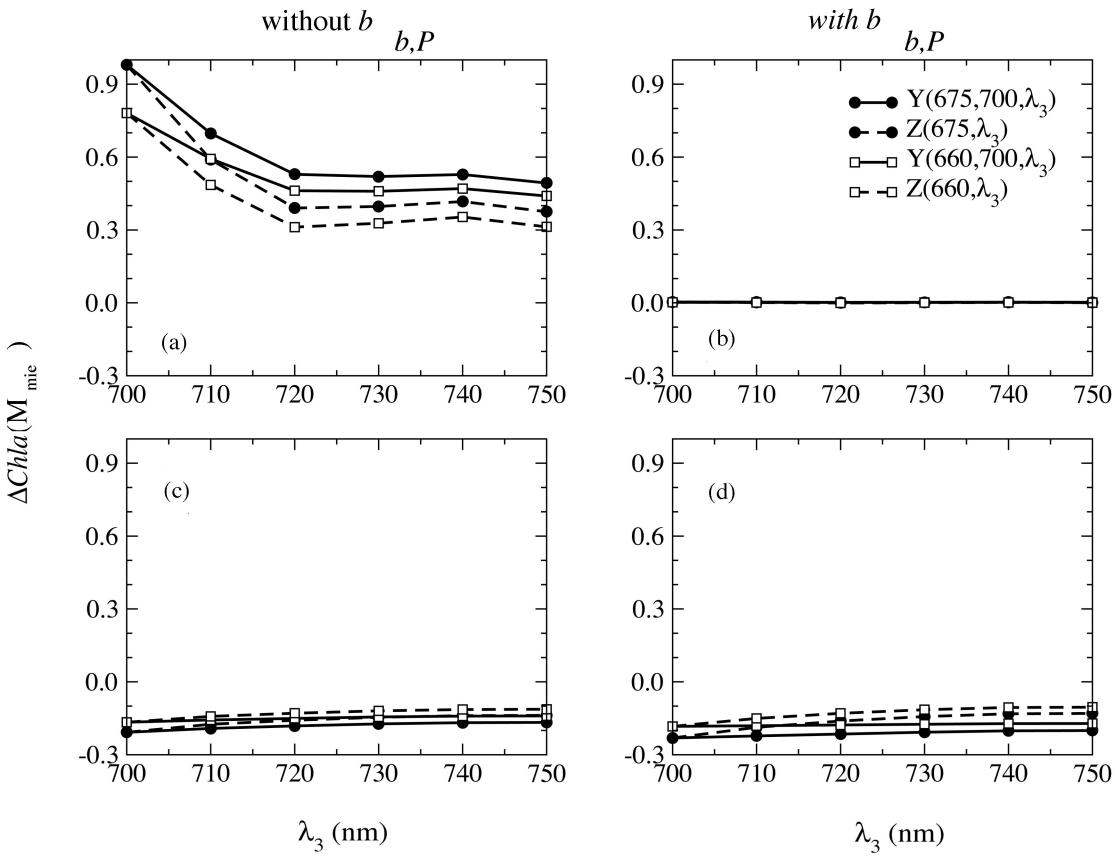

Fig. 12. $\Delta Chla$ due to changes in the phytoplankton specific inherent optical properties computed neglecting (top column) and taking into account (second column) the contribution of nonalgal particles to the total backscattering coefficient. Top row, only changes in $b_{b,\phi}^*$ are considered; bottom row, only changes in a_ϕ^* are considered.

variability of the phytoplankton specific absorption coefficient, assuming that $b_{b,\phi}$ is not a dominant component of b_b. Δa_ϕ^* is responsible for both the hump shape and the sharp decrease of $\Delta Chla$ as λ_3 shifts from 700 to 750 nm [Figs. 5(b), 5(c), 6(b), 6(c), 7(b), and 7(c)]. Variations in parameters such as $b_{b,P}^*$, a_{nap}^*, P, or ε seem to be less important compared with that of a_ϕ^*, even though they can be responsible for a peak near $\lambda_3 = 700$ nm [Figs. 6(h), 6(i), 6(k), 6(l), 8, 9(e), and 9(f)].

The variability of the chlorophyll-a fluorescence quantum yield can solely be responsible for the STE hump shape centered in the vicinity of the emission maximum (i.e., $\lambda_1 = 685$ nm) and not for the mentioned decrease. Moreover, had η been a major factor in influencing the STE, the strong λ_3 dependence found for $\Delta Chla(Z_\eta)$ at $\lambda_1 = 650$ nm [Fig. 6(f)] would have probably been more evident for the band-ratio algorithm.

In the case in which $b_{b,\phi}$ contributes significantly to $b_{b,P}$, the observed STE may be also explained by the combined variations in the phytoplankton specific inherent optical properties (Figs. 11 and 12). In such a situation, $\Delta b_{b,\phi}^*$ may be the major contributor to $\Delta Chla$.

The disappearance of the STE hump in the band ratio as $\lambda_3 \rightarrow 750$ nm seems to be due to the higher sensitivity of Z to the other parameters when λ_3 shifts toward 750 nm [Figs. 6(h)–6(o), 8, and 9(d)–9(f)]. Finally, the increase in the STE as λ_1 shifts toward 650 nm may be explained by uncertainties in a_{nap}^* and y as well as by the variability of accessory pigments (e.g., chlorophyll-b, phycocyanin) that has not been considered in this study.

In conclusion, the presented simulations suggested that the variability of the phytoplankton specific inherent optical properties may be one of the most important contributors to the accuracy of *Chla* estimation by use of Eqs. (1) and (2). However, whether the observed STE is due to variations of $b_{b,\phi}^*$ or a_ϕ^* remains unknown at this stage, also because of the lack of *in situ* spectral backscattering measurements.

7. Discussion

This study has dealt with the analysis of the sensitivity of two *Chla* algorithms to variations in bio-optical parameters and to uncertainties in R_{rs} measurements. Simulation results, obtained for realistic ranges of parameters, suggest that the variability of the phytoplankton specific absorption coefficients may be the most important source of uncertainty in *Chla* retrieval in turbid productive waters. A variation of 50% in a_ϕ^* caused errors in *Chla* of the order of 80%–100% [Figs. 5(b), 5(c), 6(b), 6(c),

7(b), and 7(c)]. In contrast, variations in $b_{b,P}$* up to 100% caused changes in *Chla* of 40% [Figs. 5(k), 5(l), 6(k), 6(l), 7(k), and 7(l)]. This behavior is expected since the algorithms are designed to extract $a_\phi(\lambda_1)$ from R_{rs} by minimizing the effects of b_b. Uncertainties in R_{rs} measurements, resulting from atmospheric correction or skylight reflection, can also contribute significantly to the error in *Chla* estimation: Changes in R_{rs} of the order of 10% caused variations in the predicted *Chla* of ~20% (Fig. 9). Instead, large variations in η (a factor of 20) and a_{nap}*(443) (a factor of 4) caused errors in *Chla* of 100% and 40%, respectively [Figs. 5(e), 5(f), 5(h), 5(i), 6(e), 6(f), 6(h), 6(i), 7(e), 7(f), 7(h), and 7(i)]. Note also that, because a_{nap} and a_{CDOM} have similar spectral shapes, variations in a_{CDOM} would cause errors in the *Chla* estimation similar to those that were due to variations in a_{nap}*(443) (not shown). Thus the results presented here do not conform with our previous conclusions, which were based only on experimental data,[1] that attributed most of the spectral dependence of the STE to variations in η.

For the same *Chla*, the concentration of total suspended particles (*P*) varied in our experimental data set by one order of magnitude[1]; thus we let *P* vary over such a range in our simulations (Table 1). As a consequence of this variation, R_{rs} changed in magnitude by approximately a factor of 7 in the red and NIR spectral regions; the shape of the spectra resembled that found in turbid estuaries (e.g., Ref. 17). Nevertheless, variations in the *Chla* predicted by Eqs. (1) and (2) in selected spectral regions (i.e., $\lambda_1 = 676$ nm and $700 \le \lambda_3 \le 750$ nm) were relatively small: In the best case $\Delta Chla(Y) \approx 10\%$ [Fig. 8(e)]. These reduced $\Delta Chla$ confirmed the ability of algorithms based on band ratios to compensate for large variations in R_{rs}.

The analysis also demonstrated that the relative importance of each parameter may change considerably both in magnitude and spectral location at different *Chla* levels. The most striking examples of this phenomenon were found for variations in the backscattering slope and in *P* that increased drastically in importance as *Chla* decreased [compare Figs. 5(n) and 5(o) with Figs. 7(n) and 7(o), and see Fig. 8].

Simulations based on specific inherent optical properties of phytoplankton, derived by use of Mie theory, demonstrated that variations in $b_{b,\phi}$* may cause errors in *Chla* larger than those that are due to variations in a_ϕ*, when $b_{b,\phi}$ dominates b_b (Fig. 12). On the other hand, variations in a_ϕ* are by far more important than those in $b_{b,\phi}$* when nonalgal particle backscattering is dominant (Fig. 12). As a final note we should stress that the homogeneous model used for representing phytoplankton cells in Mie simulations does not reproduce reliably the observed phytoplankton backscattering coefficients (see for example Ref. 29). Thus the results presented on the effect of anomalous diffraction on the variability of $b_{b,\phi}$* should be interpreted cautiously.

The results of this study can be also exploited for clarifying the differences between the three-band and ratio algorithms. On the one hand, it has been shown that the three-band algorithm (*Y*) has lower sensitivity to *Chla* than the band-ratio algorithm (*Z*) (Fig. 3). Moreover, the three-band algorithm appeared to be more sensitive to variations in the bio-optical parameters that might have the largest influence on the accuracy of *Chla* estimation, i.e., the specific inherent optical properties of phytoplankton [Figs. 5(b), 5(c), 6(b), 6(c), 7(b), 7(c), 11, and 12]. On the other hand, *Y* appeared to be slightly less sensitive than *Z* to variations in the spectral slope of $b_{b,P}$ (especially at low *Chla*), in $b_{b,P}$* and in a_{nap}* [Figs. 5(h), 5(i), 5(k), 5(l), 5(n), 5(o), 6(h), 6(i), 6(k), 6(l), 6(n), 6(o), 7(h), 7(i), 7(k), 7(l), 7(n), and 7(o). In addition, *Y* was demonstrated to be more resistant than *Z* to variations in the concentration of total suspended particles, especially at low and moderate *Chla* (Fig. 8).

The results of this study are significant for the identification of the optimal spectral regions for estimating *Chla* by use of Eqs. (1) and (2). In practice, it is not feasible to specify precisely the optimal positions of λ_1 and λ_3 to be used in the algorithms, because they depend on the relative importance of the interferences and on the trophic status of the water body. However, some recommendations can be proposed. In the hypothetical case in which interferences were not present, we would suggest selecting the regions where the algorithms are maximally sensitive to *Chla*, i.e., $\lambda_1 = 678$ nm and $\lambda_3 > \lambda_{peak}$, according to the trophic status of the water body under examination. This slightly disagrees with the previous suggestion to set $\lambda_3 = \lambda_{peak}$ (Refs. 4 and 5).

In the more realistic case, in which interferences that are due to variable bio-optical parameters and reflectance errors are not negligible, a higher accuracy in *Chla* prediction will be obtained when λ_1 is shifted to a spectral region where the algorithms are less sensitive to *Chla*, but also less sensitive to variations in bio-optical parameters and reflectance uncertainties; the region $660 \le \lambda_1 \le 670$ nm seems to be the least sensitive to the interferences considered in this study. As *Chla* increases, λ_{peak} and the λ_3 region of maximal sensitivity to *Chla* shift toward longer wavelengths, but the position of λ_3 with minimal sensitivity to variations in a_ϕ* is almost insensitive to variations in the trophic status of the water body. This suggests that in eutrophic waters an optimal spectral region for λ_3 could be found near 720–740 nm. Therefore, λ_1 = 660–670 nm and λ_3 = 720–740 nm may be considered as optimal spectral regions for estimating *Chla* in turbid productive waters using Eqs. (1) and (2). This rather large gap between λ_1 and λ_3 is supported by both our simulations and by our experimental data set collected over a wide range of optical parameters.[1] Moreover, our analysis is consistent with, and provides a biophysical explanation for, the discrepancies between the original suggestion for the optimal band locations[4,5] and those reported by numerous empirical studies.[8–14] Specifically, we demonstrated that the optimal λ_1 is located at wavelengths shorter than the *Chla* red absorption maximum and the optimal λ_3 at

wavelengths longer than λ_{peak}. For λ_3 fixed at 700 nm, shifting λ_1 from 678 to 665 nm decreased the experimental STE of Z from 22 to 15 mg m^{-3}, while, for $\lambda_1 = 678$ nm, shifting λ_3 from 700 to 730 nm reduced the STE down to 11 mg m^{-3} (Fig. 1). Finally, the STE obtained for $\lambda_1 = 665$ nm and $\lambda_3 = 730$ nm reached a value of 8 mg m^{-3} and therefore it was reduced by more than a factor of 2.

Appendix A: Semianalytical Model for Simulating Reflectance Spectra

The model of Kattawar and Vastano[15] [their Eq. (13)] was used to simulate the subsurface irradiance reflectance of an infinitely deep homogeneous water body. This model accounts for chlorophyll-a inelastic scattering, and it requires as input parameters the spectral total absorption, scattering, and backscattering coefficients, as well as the chlorophyll-a fluorescence quantum yield (η), and the just below-surface downward irradiance. The model was parameterized as follows.

The spectral total absorption coefficient was expressed as

$$a = a_\phi + a_{\text{nap}} + a_{\text{CDOM}} + a_w, \tag{A1}$$

where a_ϕ, a_{nap}, a_{CDOM}, and a_w are the absorption coefficients of phytoplankton, nonalgal particles, colored dissolved organic matter, and pure water, respectively.

The phytoplankton absorption coefficient was obtained as the product of the specific absorption coefficient (a_ϕ^*) and the chlorophyll-a concentration, i.e., $a_\phi = a_\phi^* Chla$. To include the dependency of a_ϕ^* on the packaging effect, we used the theory that was developed for monodispersed spherical cells[19]:

$$a_\phi^* = \frac{3}{2}\, a_{\text{sol}}^* \frac{Q_a(\rho')}{\rho'}, \tag{A2}$$

where Q_a is the efficiency factor for absorption:

$$Q_a(\rho') = 1 + \frac{2e^{-\rho'}}{\rho'} + 2\,\frac{e^{-\rho'} - 1}{\rho'^2}, \tag{A3}$$

and ρ' is a parameter that combines the size parameter ($\alpha = \pi d/\lambda$) with the imaginary part of the refractive index (n'):

$$\rho' = 4\alpha n' = a_{\text{sol}}^* c_i d, \tag{A4}$$

where a_{sol}^* is the idealized specific absorption coefficient for pigments in solution, c_i is the intracellular pigment concentration, and d is the diameter of the spherical cell.[18]

A theoretical a_{sol}^* spectrum was calculated from our experimental data,[1] as $a_{\text{sol}}^* = 10(a_\phi^*)^{1.45}$, where the constant 1.45 was selected so that $a_{\text{sol}}^*(676) \approx 0.04$ m^2 mg^{-1} (see for example Ref. 30). Then, we set c_i to 2.86×10^6 mg mg^{-3} (Ref. 28) and we computed a_ϕ^* by using Eq. (A2) by setting $d = 15$ μm to obtain the simulated phytoplankton specific absorption coefficient at 678 nm equal to the one measured, i.e., $a_\phi^*(678) = 0.023$ m^2 mg^{-1} (Ref. 1). The theoretical and measured a_ϕ^* were in good agreement between 450 and 800 nm (root-mean-square error $= 7 \times 10^{-4}$ m^2 mg^{-1}); the simulated a_ϕ^* underestimated the measured a_ϕ^* in the blue region (<450 nm, root-mean-square error $= 9 \times 10^{-3}$ m^2 mg^{-1}) (Fig. 13).

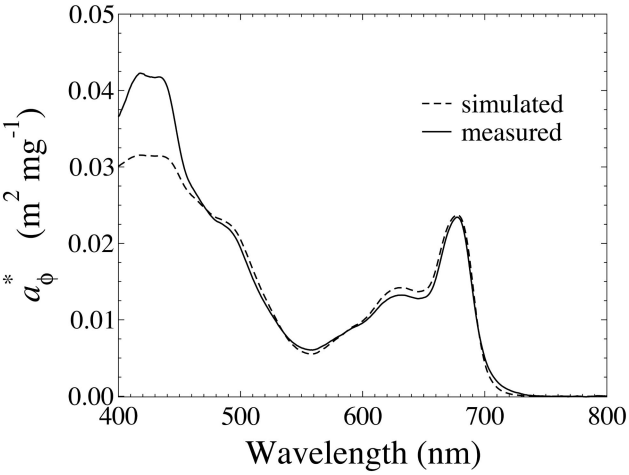

Fig. 13. Simulated (dashed curve) phytoplankton specific absorption coefficient compared with the measured one (solid curve).

We expressed a_{nap} and a_{CDOM} as exponentially decreasing functions of wavelength[17,31]:

$$a_{\text{nap}}(\lambda) = a_{\text{nap}}(443)\exp[-S_{\text{nap}}(\lambda - 443)], \tag{A5}$$

$$a_{\text{CDOM}}(\lambda) = a_{\text{CDOM}}(440)\exp[-S_{\text{CDOM}}(\lambda - 440)]. \tag{A6}$$

The slope $S_{\text{nap}} = 0.0123$ nm^{-1} was taken from Babin *et al.*,[17] while $S_{\text{CDOM}} = 0.014$ nm^{-1} was obtained from Ref. 31. To account for the observed covariation between a_{nap} and $Chla$, $a_{\text{nap}}(443)$ was expressed as $a_{\text{nap}}(443) = (0.031)(0.81)Chla$, where 0.031 and 0.81 are the mass-specific a_{nap} coefficient and the P:$Chla$ ratio, respectively, and P is the total suspended particle concentration.[17] We used the water absorption coefficient that was published by Buiteveld and collaborators.[31] The total backscattering coefficient, b_b, was expanded as

$$b_b(\lambda) = b_{b,P}(\lambda) + b_{b,w}(\lambda), \tag{A7}$$

where $b_{b,P}$ and $b_{b,w}$ are the backscattering coefficients of all suspended particles and of pure water, respectively. $b_{b,P}$ was expressed as

$$b_{b,P}(\lambda) = b_{b,P}^*(550)\left(\frac{\lambda}{550}\right)^y P, \tag{A8}$$

where $b_{b,P}^*(550) = 0.0086$ m^2 g^{-1} (Ref. 16) is the spe-

cific backscattering coefficient of suspended particles, y is the spectral slope of $b_{b,P}$ (arbitrarily set to 0). As suggested by Morel,[32] $b_{b,w}$ was expressed as

$$b_{b,w}(\lambda) = 0.0011\left(\frac{\lambda}{550}\right)^{-4.32}. \quad \text{(A9)}$$

Assuming a particle backscattering efficiency ($b_{b,P}/b_P$) equal to that measured by Petzold in turbid harbor waters,[33] and using the volume scattering function of pure water,[32] we computed the total scattering coefficient as

$$b(\lambda) = b_{b,P}(\lambda)/0.02 + b_{b,w}(\lambda)/0.5. \quad \text{(A10)}$$

We computed the above-surface downward irradiance, $E_d(0+, \lambda)$, as proposed by Gege[34] by setting the parameters of his model as follows: $\alpha = 0.4$, $\beta = 0.1$, $\gamma = 0.1$, $\delta = 0$, and $\nu = 0$. Here α, β, γ, and δ are the fractions of the four sources of E_d, i.e., the direct solar radiation, the blue sky radiation and the radiations of aerosol scattering, and clouds, respectively; ν is the exponent describing the aerosol scattering wavelength dependence (See Ref. 34 for further details). We computed below-surface downward irradiance as $E_d(0+, \lambda) = E_d(0+, \lambda)t(a, w) + E_u(0-, \lambda)r(w, a)$, where we considered $E_u(0-, \lambda)r(a, w)$ negligible and $t(w, a) = 0.98$ (Ref. 35). We finally converted the subsurface irradiance reflectance into above-surface remote-sensing reflectance following Mobley[35] [Eq. (10.27), setting $t(w, a) = 0.98$, $t(a, w) = 0.96$, $r(w, a) = 0.5$, $n = 1.33$, and $Q = 4$; e.g., Ref. 22]. The chlorophyll-a fluorescence emission function was approximated by a Gaussian peak centered at 685 nm with a standard deviation of 10.6 nm.[35]

To carry out the analysis we set the parameters to typical values found in turbid productive water by using our experimental data set[1] and published data (Table 1).

This study was supported by U.S. Environmental Protection Agency, contract number R-828634501. G. Dall'Olmo was supported by NASA Headquarters under Earth System Science Fellowship grant NGT5-NNG04GQ82H. The use of the facilities of the Center for Advanced Land Management Information Technologies is gratefully acknowledged. We also kindly thank E. Boss and W. Clavano for providing the code for Mie calculations. Finally we thank three anonymous reviewers and Z. P. Lee for their pertinent comments that greatly improved this manuscript. This research is a contribution of the University of Nebraska Agricultural Research Division, Lincoln, Nebraska. This research was supported in part by funds provided through the Hatch Act.

References

1. G. Dall'Olmo and A. A. Gitelson, "Effect of bio-optical parameter variability on the remote estimation of chlorophyll-a concentration in turbid productive waters: experimental results," Appl. Opt. **44,** 412–422 (2005). See also erratum in **44,** 3342 (2005).
2. A. Gitelson, G. Keydan, and V. Shishkin, "Inland water quality assessment from satellite data in visible range of the spectrum," Sov. Remote Sens. **6,** 28–36 (1985).
3. A. Gitelson, K. Kondrat'ev, and G. Garbusov, "New approach to monitoring aquatic ecosystem quality," Trans. USSR Acad. Sci. **295,** 825–827 (1987).
4. A. A. Gitelson and K. Y. Kondratyev, "Optical models of mesotrophic and eutrophic water bodies," Int. J. Remote Sens. **12,** 373–385 (1991).
5. A. G. Dekker, "Detection of optical water quality parameters for eutrophic waters by high resolution remote sensing," Ph.D. thesis (Vrije Universiteit, 1993).
6. S. Thiemann and H. Kaufmann, "Lake water quality monitoring using hyperspectral airborne data—a semiempirical multisensor and multitemporal approach for the Mecklenburg Lake District, Germany," Remote Sens. Environ. **81,** 228–237 (2002).
7. H. J. Hoogenboom, A. G. Dekker, and I. A. Althuis, "Simulation of aviris sensitivity for detecting chlorophyll over coastal and inland waters," Remote Sens. Environ. **65,** 333–340 (1998).
8. D. Pierson and N. Strömbäck, "A modelling approach to evaluate preliminary remote sensing algorithms: Use of water quality data from Swedish great lakes," Geophysica **36,** 177–202 (2000).
9. K. Oki and Y. Yasuoka, "Estimation of chlorophyll concentration in lakes and inland seas with a field spectroradiometer above the water surface," Appl. Opt. **41,** 6463–6469 (2002).
10. E. F. Hoge and C. W. S. N. R. Wright, "Radiance-ratio algorithm wavelengths for remote oceanic chlorophyll determination," Appl. Opt. **26,** 2082–2094 (1987).
11. K. Kallio, T. Kutser, T. Hannonen, S. Koponen, J. Pulliainen, J. Veps, and T. Pyh, "Retrieval of water quality from airborne imaging spectrometry of various lake types in different seasons," Sci. Total Environ. **268,** 59–77 (2001).
12. J. Pulliainen, K. Kallio, K. Eloheimo, S. Koponen, H. Servomaa, T. Hannonen, S. Tauriainen, and M. Hallikainen, "A semi-operative approach to lake water quality retrieval from remote sensing data," Sci. Total Environ. **268,** 79–93 (2001).
13. K. Kallio, S. Koponen, and J. Pulliainen, "Feasibility of airborne imaging spectrometry for lake monitoring—a case study of spatial chlorophyll alpha distribution in two meso-eutrophic lakes," Int. J. Remote Sens. **24,** 3771–3790 (2003).
14. P. Ammenberg, P. Flink, T. Lindell, D. Pierson, and N. Strombeck, "Bio-optical modelling combined with remote sensing to assess water quality," Int. J. Remote Sens. **23,** 1621–1638 (2002).
15. G. W. Kattawar and J. C. Vastano, "Exact 1-D solution to the problem of chlorophyll fluorescence from the ocean," Appl. Opt. **21,** 2489–2492 (1982).
16. D. A. Kiefer and R. A. Reynolds, "Advances in understanding phytoplankton fluorescence and photosynthesis," in *Primary Productivity and Biogeochemical Cycles in the Sea*, P. G. Falkowsky and A. D. Woodhead, eds. (Plenum, 1992), pp. 155–174.
17. M. Babin, D. Stramski, G. M. Ferrari, H. Claustre, A. Bricaud, G. Obolensky, and N. Hoepffner, "Variations in the light absorption coefficients of phytoplankton, nonalgal particles, and dissolved organic matter in coastal waters around Europe," J. Geophys. Res. Oceans **108,** 3211 (2003).
18. A. Albert and C. D. Mobley, "An analytical model for subsurface irradiance and remote sensing reflectance in deep and shallow case-2 waters," Opt. Exp. **11,** 2873–2890 (2003).
19. A. Morel and A. Bricaud, "Theoretical results concerning light absorption in a discrete medium, and application to specific absorption of phytoplankton," Deep-Sea Res. **28A,** 1375–1393 (1981).
20. A. Vasilkov and O. Kopelevich, "Reasons for the appearance of

the maximum near 700 nm in the radiance spectrum emitted by the ocean layer," Oceanology **22,** 697–701 (1982).
21. H. Loisel and A. Morel, "Non-isotropy of the upward radiance field in typical coastal (case 2) waters," Int. J. Remote Sens. **22,** 275–295 (2001).
22. Y. J. Park and K. Ruddick, "Model of remote-sensing reflectance including bidirectional effects for case 1 and case 2 waters," Appl. Opt. **44,** 1236–1249 (2005).
23. C. D. Mobley, "Estimation of the remote-sensing reflectance from above-surface measurements," Appl. Opt. **38,** 7442–7455 (1999).
24. K. G. Ruddick, F. Ovidio, and M. Rijkeboer, "Atmospheric correction of SeaWiFS imagery for turbid coastal and inland waters," Appl. Opt. **39,** 897–912 (2000).
25. H. C. van de Hulst, *Light Scattering by Small Particles* (Wiley, 1957).
26. C. F. Bohren and D. R. Huffman, *Absorption and Scattering of Light by Small Particles* (Wiley, 1983).
27. A. Bricaud and A. Morel, "Light attenuation and scattering by phytoplanktonic cells: a theoretical modeling," Appl. Opt. **25,** 571–580 (1986).
28. R. P. Bukata, J. H. Jerome, J. E. Bruton, and S. C. Jain, "Determination of inherent optical properties of Lake Ontario coastal waters," Appl. Opt. **18,** 3926–3932 (1979).
29. R. D. Vaillancourt, C. W. Brown, R. R. L. Guillard, and W. M. Balch, "Light backscattering properties of marine phytoplankton: relationships to cell size, chemical composition and taxonomy," J. Plankton Res. **26,** 191–212 (2004).
30. A. Bricaud, H. Claustre, J. Ras, and K. Oubelkheir, "Natural variability of phytoplanktonic absorption in oceanic waters: influence of the size structure of algal populations," J. Geophys. Res. Oceans **109,** (2004).
31. A. Briraud, A. Morel, and L. Prieur, "Optical efficiency factors of some phytoplankters," Limnol. Oceanogr. **28,** 816–832 (1983).
32. H. Buiteveld, J. H. M. Hakvoort, and M. Donze, "The optical properties of pure water," in *Ocean Optics XII,* SPIE **2258,** (1994).
33. A. Morel, "Optical properties of pure water and pure seawater," in *Optical Aspects of Oceanography,* Jerlov and E. Steeman Nielsen, eds. (Academic, 1974).
34. T. J. Petzold, "Volume scattering functions for selected ocean waters," in *Light in the Sea,* J. E. Tyler, Dowden, Hutchinson, Ross, and Stroudsberg, eds. (Scripps Institute of Oceanography, 1977).
35. P. Gege, "The water color simulator Wasi: An integrating software tool for analysis and simulation of optical in situ spectra," Comput. Geosci. **30,** 523–532 (2004).
36. C. D. Mobley, *Light and Water: Radiative Transfer in Natural Waters* (Academic, 1994).